

Observing the air-sea turbulent heat flux on the trajectory of tropical storm Danas*

Xuehan XIE^{1,2,**}, Xiangzhou SONG^{1,2}, Marilena OLTMANN³, Yangang LI⁴,
Qifeng QIAN⁵, Zexun WEI⁶

¹Key Laboratory of Marine Hazards Forecasting, Ministry of Natural Resources, Hohai University, Nanjing 210098, China

²College of Oceanography, Hohai University, Nanjing 210098, China

³National Oceanography Centre, Southampton SO14 3ZH, United Kingdom

⁴East China Sea Forecasting and Disaster Reduction Center, Ministry of Natural Resources, Shanghai 200136, China

⁵National Meteorological Centre, China Meteorological Administration, Beijing 100081, China

⁶First Institute of Oceanography, Ministry of Natural Resources, Qingdao 266061, China

Received Sep. 23, 2023; accepted in principle Oct. 5, 2023; accepted for publication Jan. 4, 2024

© Chinese Society for Oceanology and Limnology, Science Press and Springer-Verlag GmbH Germany, part of Springer Nature 2024

Abstract Tropical cyclones constitute a major risk for coastal communities. To assess their damage potential, accurate predictions of their intensification are needed, which requires a detailed understanding of the evolution of turbulent heat flux (THF). By combining multiple buoy observations along the south-north storm track, we investigated the THF anomalies associated with tropical storm Danas (2019) in the East China Sea (ECS) during its complete life cycle from the intensification stage to the mature stage and finally to its dissipation on land. The storm passage is characterized by strong winds of 10–20 m/s and a sea level pressure below 1 000 hPa, resulting in a substantial enhancement of THF. Latent heat (LH) fluxes are most strongly affected by wind speed, with a gradually increasing contribution of humidity along the trajectory. The relative contributions of wind speed and temperature anomalies to sensible heat (SH) depend on the stability of the boundary layer. Under stable conditions, SH variations are driven by wind speed, while under near-neutral conditions, SH variations are driven by temperature. A comparison of the observed THF and associated variables with outputs from the ERA5 and MERRA2 reanalysis products reveals that the reanalysis products can reproduce the basic evolution and composition of the observed THF. However, under extreme weather conditions, temperature and humidity variations are poorly captured by ERA5 and MERRA2, leading to large LH and SH errors. The differences in the observed and reproduced LH and SH during the passage of Danas amount to 26.1 and 6.6 W/m² for ERA5, respectively, and to 39.4 and 12.5 W/m² for MERRA2, respectively. These results demonstrate the need to improve the representation of tropical cyclones in reanalysis products to better predict their intensification process and reduce their damage.

Keyword: tropical cyclone (TC); air-sea turbulent heat flux (THF); latent heat flux; sensible heat flux; buoy observation; reanalysis product

1 INTRODUCTION

Tropical cyclones (TCs) are isolated strong convective weather systems that form over warm seas (temperatures above 26.5 °C) and are known as one of the most dangerous natural hazards on the planet (Bracken and Bosart, 2000; Dare and McBride, 2011; McTaggart-Cowan et al., 2015). NOAA estimates that TCs have caused over \$1.3 trillion in damage, with an average cost of \$22.8

billion per event. They are also responsible for the most deaths: 6 890 since 1980 (NOAA Office for Coastal Management, 2023). The World Meteorological Organization (WMO) classifies TCs that develop in the northwest Pacific into tropical depressions (TDs), tropical storms (TSs), severe

* Supported by the National Natural Science Foundation of China (Nos. 42122040, 42076016)

** Corresponding author: xuehanxie@hhu.edu.cn

tropical storms and typhoons based on the 10-minute average wind speed (WS) near the surface of the cyclone center (Kepert and Ginger, 2010).

TCs are characterized by intense winds and heavy precipitation and can cause storm surge disasters (Hubbert et al., 1991; Rodgers et al., 1994; Needham and Keim, 2014; Liu and Tang, 2016; Khouakhi et al., 2017). Strong wind churn causes cold water upwelling, vertical entrainment and surface buoyancy flux (including net heat fluxes and freshwater fluxes) anomalies, resulting in the cooling of sea surface temperature (SST) and the consequent formation of a cold wake along the trajectory of TCs (Price, 1981; Stramma et al., 1986; D'Asaro et al., 2007; Price et al., 2008; Ma et al., 2020). A cold wake covering a larger area can suppress local clouds and rainfall activity. In such cases, it takes several weeks for the sea surface to return to normal conditions. Karnauskas et al. (2021) found that cold wakes reduce the frequency of weak to moderate TCs but enhance the incidence of strong typhoons.

The damage potential of TCs depends mostly on their strength and size (Powell and Reinhold, 2007), which are affected by surface heat fluxes. Heat fluxes are the major source of energy for the development, intensification, and maintenance of TCs (Malkus and Riehl, 1960; Emanuel, 1986, 1995). For example, Hurricane Katrina (2005) strengthened from Category 1 to Category 5 in two days due to a warm vortex crossing the Gulf of Mexico (Scharroo et al., 2005); TS Nargis (2008) strengthened from Category 1 to Category 4 in less than 24 h in the Bay of Bengal due to subsurface warm anomalies (Lin et al., 2009). Ma et al. (2015) found that removing sensible heat fluxes resulted in a 20% reduction in TC size. Therefore, the accurate estimation of air-sea turbulent heat fluxes (THFs) leads to an improved prediction of the formation, trajectory, and intensity of TCs, which is essential for marine disaster prevention and mitigation.

In recent years, the application of satellite remote sensing and the advent of numerical weather prediction (NWP) models have rapidly improved TC trajectory predictions (Goerss et al., 2004; Landsea and Cangialosi, 2018). However, TC intensity predictions have improved slowly and remain a major challenge for operational ocean forecasting (DeMaria et al., 2005, 2014). The discrepancy between the improvement of intensity and trajectory predictions is attributed to their different drivers. TC trajectories are mainly

controlled by the large-scale air-sea environment, while TC intensity is more sensitive to uncertainties in the initial and boundary conditions, which are affected by small- and medium-scale physical processes such as internal dynamics and THFs (Marks and Houze, 1987; Zhang and Sippel, 2009; Komori et al., 2018; Jayakrishnan et al., 2020). Due to the lack of in-situ observations and uncertainties in the model parameterization, predictions of more chaotic and sensitive intensity variation processes are much less reliable than TC trajectory forecasts. Despite the remarkable development of global ocean stereoscopic observations, both direct and indirect observations have limitations for small- and medium-scale ocean hazards such as TCs, which are characterized by extreme winds and rainfall (Yelland et al., 1998; Landwehr et al., 2015; Centurioni et al., 2019; Cronin et al., 2019).

Direct measurements of THFs are expensive and extremely limited in coverage due to platform constraints. They are often located in shallow waters (e.g., flux towers), making it difficult to capture small- to medium-scale changes such as the development and rapid intensification of remotely located and highly contingent TCs. Moreover, satellite observations that are assimilated in TC forecasts provide global coverage but make it difficult to estimate THFs independently due to the lack of boundary layer meteorological variables such as temperature, humidity, and pressure. In addition, satellite observations are heavily influenced by weather events such as clouds and rain. The scarcity of in-situ observations of TCs also limits the progress of model parameterization. The estimation of THFs and the formation of reanalysis flux products are commonly based on semiempirical parametric algorithms, and their improvement cannot be achieved without a large amount of high-resolution in-situ measurements.

Buoy observations are a preferred method of estimating THF during TCs. Several systematic buoy observation networks have been established worldwide, such as the Global Tropical Moored Buoy Array (GT MBA; McPhaden, 1995). In a variety of reanalysis products, such as ERA5, MERRA2 and NCEP, as well as in many large ocean observation programs, such as GOOS (Malone, 2003) and TPOS 2020 (Smith et al., 2019), buoys have the unique advantage of complementing other observation tools (e.g., ships, flux towers, satellites) to support flux-related scientific research programs, such as JGOFS (Garrison et al., 2000)

and SOLAS (Schultz, 2011), as well as to advance the development of operational typhoon hazard forecasting. The moored and drifting buoys applied in this study enable high-resolution, continuous, all-element observations that support flux estimation. Based on a moored Bailong buoy (16.9°S, 115.2°E), Song et al. (2021) showed the full flux anomalies caused by three TCs in the southeast Indian Ocean, while Xie et al. (2022) investigated the extreme turbulent flux anomalies during the passage of TC Barijat (2018) in the South China Sea based on a new drifting buoy. Even under extreme weather conditions, buoys can provide high-resolution (hourly) observations of air-sea variables to estimate THFs. Thus, the combination of multiple buoys enables the tracking and examination of TC Danas' life cycle, which increases our understanding of the evolution and development of extreme THF anomalies.

In this study, we investigated the THF anomaly process during the life cycle of TC Danas (2019) across multiple latitudinal belts using high-precision observations from multiple moored and drifting buoys in the East China Sea (ECS). We aimed to achieve three objectives: First, to estimate the THF variation over the nearly full life cycle of the TC; second, to assess the relative contributions of the wind speed and the thermal forcing to the hourly THF anomalies during TC development; and third, to determine error sources in the existing air-sea flux products and model uncertainties. The remainder of the paper is organized as follows: Section 2 presents the buoy observations along the TC path and reanalysis flux products and describes the parametric methods for flux estimation. In Section 3, we investigate the influence of the TC on the THF anomalies observed by the buoys. We then analyze the physical mechanisms underlying the flux anomalies and their relation to the air-sea boundary layer stability (BLS). Last, we evaluated the performance of two state-of-the-art reanalysis flux products with high spatial and temporal resolutions based on buoy observations. Section 4 concludes this study with a summary and discussion.

2 MATERIAL AND METHOD

2.1 TC track dataset

We used the International Best Track Archive for Climate Stewardship (IBTrACS; Knapp et al., 2010), which was developed in collaboration with NOAA's National Climatic Data Center and the World Meteorological Data Center, to present the

TC Danas track variability (Fig.1). The IBTrACS compiles and archives historical TC best-track data from WMO Regional Specialized Meteorological Centers (RSMCs) and Tropical Cyclone Warning Centers (TCWCs), as well as from multiple national agencies, into a global dataset using a single format. This multisource product provides information on the average position of the TC, which is available every 3 h and is combined with typhoon records from the National Meteorological Center (NMC). Thus, TC Danas strengthened from a TD to a TS at 0600 UTC on 16 July 2019. TS Danas was blocked by the topography of its mountains as it moved westward close to Luzon, resulting in a rare split into two circulation centers. The new center west of Luzon gradually dissipated as a South China Sea depression, while the weaker old center around the eastern side traveled northward through the ECS. The winds strengthened slightly as the old center moved north in combination with its easterly disturbance but remained at TS levels. Danas eventually made landfall off the coast of Jeollabuk-do, South Korea, at approximately 1400 UTC on

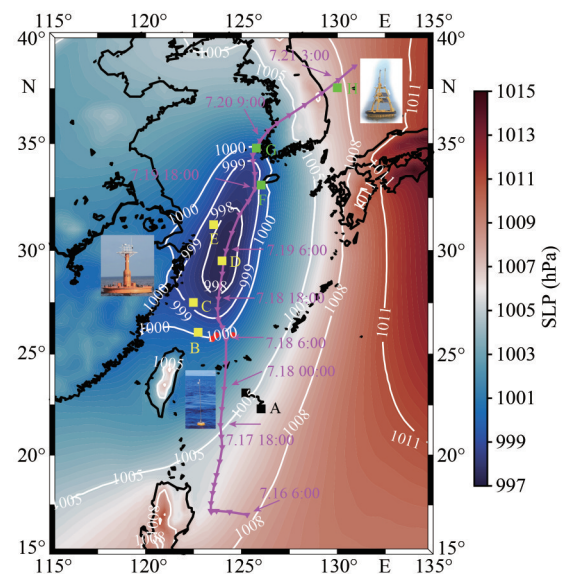


Fig.1 Map of buoy positions around the track of TS Danas based on the IBTrACS dataset

Buoy A was a drifting buoy and Buoys B–H were moored buoys. The triangles on the trajectory indicate the position of Danas every 3 h and the dates (month·day hour UTC) are incorporated along with them. The colored background shows the mean sea level pressure (SLP, unit: hPa) from the ERA5 field during the passage of Danas (July 16–20), with the white isobars below 1000 hPa highlighting the influence of tropical storm (TS) Danas. Land and island outlines are indicated by black lines. The red dots indicate the location of the Diaoyu Island, Huangwei Yu, and Chiwei Yu from left to right.

20 July. Danas then crossed Korea into the Sea of Japan as a TD and continued northward, gradually weakening into an extratropical cyclone.

2.2 Buoy observation

To quantify the dramatic intensification during the TS development phase, we screened several near-track buoys, the details of which are listed in Table 1. Buoys A–E belong to the State Oceanic Administration (SOA), China. They have a complete set of variable observations for estimating THF, including WS, SST, surface air temperature (SAT), sea level pressure (SLP) and relative humidity (RH). Drifting Buoy A outputs data 8 times per hour, Mooring Buoys B and D output data every half hour, and Mooring Buoys C and E output data every 10 min. We collected data from moored Buoys F–H from the National Data Buoy Center (NDBC), supplied by the Korea Meteorological Administration. They provide WS, SLP, RH and temperature information hourly. These high temporal resolution buoys can be used to observe the diurnal variability of the air-sea interface. Observations from Buoys A–H lasted from 17 to 21 July and covered the life cycle of the northbound Danas from a TS to a TD around the time of landfall. Of these, Buoys A–G captured TS Danas. By the time it reached Buoy H, Danas had weakened to TD (Fig.1).

2.3 High-resolution reanalysis flux product

To improve forecast systems and prevent future damages associated with TCs, the performance of available forecast systems is evaluated against in-situ observations. Thus, two state-of-the-art reanalysis flux products available were selected. The European Centre for Medium-Range Weather Forecasts (ECMWF) Reanalysis Version 5 (ERA5; Hersbach et al., 2020) provides hourly estimates of atmospheric, surface, and oceanic variables from

1940 to the present (Bell et al., 2021). ERA5 is an improved version of ERA-Interim (Dee et al., 2011), which has the advantage of having better TC simulations. However, the SST estimates in ERA5 do not include diurnal variations. The other product is Modern-Era Retrospective Analysis for Research and Applications Version 2 (MERRA2; Gelaro et al., 2017) from NASA's Global Modeling and Assimilation Office (GMAO), which provides hourly air-sea variables from 1980 to the present. ERA5 and MERRA2 are gridded products with spatial resolutions of $0.25^{\circ} \times 0.25^{\circ}$ and 0.625° (longitude) $\times 0.5^{\circ}$ (latitude) respectively. Their hourly output can capture finer details of oceanic and atmospheric phenomena.

In this study, we evaluated these reanalysis products using multiple high-precision buoy observations, as shown in Section 3.2 and Supplementary Files S1–S4. Furthermore, to enhance the efficiency of operational forecasting, ERA5 and MERRA2 applied the Louis 79 scheme (Louis, 1979) to assimilate multisource air-sea observations. This scheme is simpler than the Coupled Ocean-Atmosphere Response Experiment Version 3.5 (COARE 3.5) algorithm, which is commonly used for parametric in-situ observations and is used in this study. We obtained recalculated reanalysis flux results based on the COARE 3.5 algorithm using the reanalysis air-sea parameters to avoid algorithm differences affecting the reasonableness of the assessment. Supplementary File S4 shows that there is a high correlation between the recalculated reanalysis fluxes and the fluxes provided directly by the reanalysis. Therefore, the assessment can be considered reasonable.

2.4 Bulk formula for estimating THF

Based on the Monin-Obukhov similarity theory (Monin and Obukhov, 1954), the COARE 3.5 algorithm was applied for the parametric estimation

Table 1 Information on drifting buoy A and mooring buoys B–H

Buoy code	Location	Parameter	Temporal resolution	Source
A	22.3°N–23.1°N, 125.2°W–126.1°W		8 times/h	
B	26.1°N, 122.7°W		30 min	State Oceanic Administration (SOA), China
C	27.5°N, 122.5°W		10 min	
D	29.5°N, 124.0°W	Wind speed (WS); sea level pressure (SLP); sea surface temperature (SST); surface air temperature (SAT); relative humidity (RH)	30 min	
E	31.2°N, 123.5°W		10 min	
F	33.1°N, 126.0°W			
G	34.8°N, 125.8°W		Hourly	Korea Meteorological Administration
H	37.5°N, 130.0°W			

of latent heat (LH) and sensible heat (SH). The equations are commonly called bulk formulas (Liu et al., 1979; Fairall et al., 2003; Edson et al., 2013) and can be expressed as:

$$Q_{\text{LH}} = \rho L_c C_E \left| \vec{u}_z \right| (q_s - q_a), \quad (1)$$

$$Q_{\text{SH}} = \rho C_p C_H \left| \vec{u}_z \right| (T_s - T_a), \quad (2)$$

where Q_{LH} and Q_{SH} on the left-hand side (lhs) represent LH and SH, respectively; ρ is the air density; L_c is the LH of evaporation; C_p is the air specific heat at constant pressure; C_E and C_H represent the turbulent exchange coefficients of LH and SH, respectively; $\left| \vec{u}_z \right|$ is the WS at height z ; $\Delta q = q_s - q_a$ and $\Delta T = T_s - T_a$ represent air-sea specific humidity and temperature differences, respectively; and the subscript s denotes the sea surface and the subscript a denotes the surface air. Since the buoys used in this study are not capable of measuring current velocity, u_z indicates absolute velocity. Song (2020) assessed the impact of sea surface currents (SFCs) on the estimation of THFs. We assume that the effect of SFCs on this study is negligible.

2.5 Parameter z/L for determining the BLS conditions

The BLS is closely related to the physical mechanisms of variation in THFs and can be determined using the Monin-Obukhov stability parameter $\zeta = z/L$, where z is the height of the turbulent exchange coefficient; the Obukhov length scale L reflects the ratio of work done by the Reynolds stress to that done by the buoyancy force within the boundary layer (Godfrey and Beljaars, 1991; Fairall et al., 1996):

$$L = T_v \frac{u_*^2}{\kappa g [(1 + 0.61) q_a T_*^2 + 0.61 T_a q_*]}, \quad (3)$$

where $\kappa \approx 0.4$ is the von Kármán constant; g is the acceleration gravitational constant; u_* , T_* , and q_* represent the scaling parameters (Eq.9 in Fairall et al., 1996); and T_v is the air virtual temperature. The boundary layer is unstable, near-neutral, and stable in the cases of $z/L < -0.4$, $-0.4 < z/L < 0.1$, and $z/L > 0.1$, respectively.

3 RESULT

3.1 THF anomalies and their physical mechanisms based on buoy observations

Figure 2 shows the air-sea variable during the

northward movement of Danas as observed by Buoys A–H. The three-stage averages along with two rates of increase for the air-sea variables are shown in Fig.3. From July 17 to 21, TC Danas resulted in a general increase in WS from an average of 6 m/s to over 10 m/s, as shown in Figs.2a & 3a. TS Danas was at maturity as it approached Buoys C–F, where a maximum WS of 20 m/s was observed at Buoy F, and maximum WS increases of 83% and -61% were observed as Danas passed Buoys E–F. The weakening of Danas from a TS to a TD upon landfall was accompanied by an increase in surface friction, as the extreme mean WS measured by Buoy G was reduced to 7 m/s. The WS associated with TD Danas returned to above 10 m/s as it crossed the land and traveled back into the sea, at which point it gradually weakened into an extratropical cyclone. The passage of Danas caused a dramatic decrease in SLP to a minimum of 982 hPa, as measured by Buoy D (Fig.2b). This decrease may have captured the low-pressure environment of the typhoon eye. SST and SAT variability are constrained by latitude. Figure 2c shows that Danas developed in low-latitude oceans with an SST > 29.7 °C and gradually weakened as it reached high-latitude waters with an SST < 23.1 °C. On the other hand, cooling of low heat capacity air occurs during upward expansion, so the SAT in extreme cyclone conditions is 0.1–0.9 °C lower than that in calm weather conditions (Fig.2d). Additionally, the RH was lower during Danas than during calm weather, decreasing by approximately 0.1%–3.2% (Fig.2e). From Buoy B to Buoy E, the water vapor content increased with the growing intensity of TS Danas, with extreme average RH values of 84.3%, 88.5%, 90.8%, and 93.3%, respectively (Fig.3e). Δq is closely related to SST and therefore also has a latitudinal characteristic. Figure 2f shows that the extreme mean Δq at Buoy A was 5.1 g/kg and then decreased sequentially with increasing latitude thereafter, except at Buoy F, where the wind field was strongest, and at Buoy H, where Danas returned to the sea surface. The extremely high anomalies in the rate of increase at Buoy E were due to fluctuations in Δq around zero (Fig.3f).

Intense LH release and SH exchange occurred at the air-sea interface due to the combined effects of the WS anomalies and the surface specific humidity-related SST anomalies induced by TC Danas (Fig.2g & h). Figure 3g & h shows that the highest extreme mean LH and SH values of 202 and 29 W/m², respectively, were observed at Buoy A under the

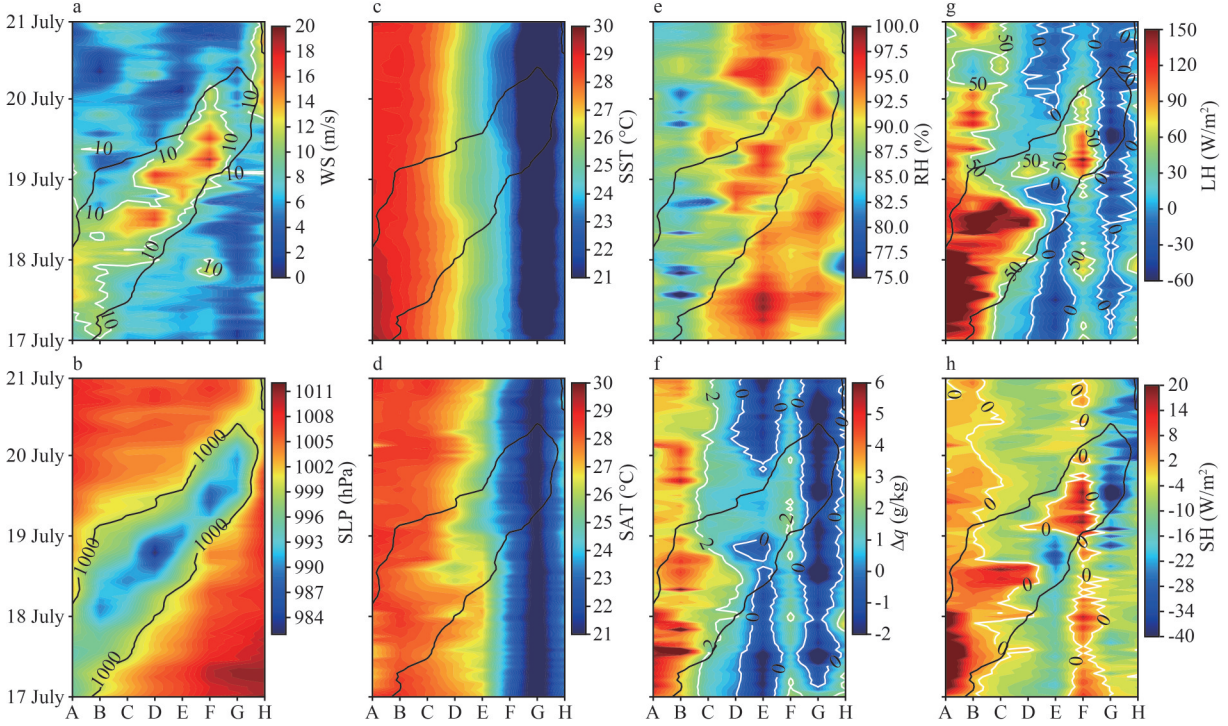


Fig.2 Changes in air-sea parameters observed by Buoy A–H distributed along the track of TC Danas

Air-sea parameters include: a. wind speed (WS, unit: m/s); b. sea level pressure (SLP, unit: hPa); c. sea surface temperature (SST, unit: °C); d. surface air temperature (SAT, unit: °C); e. relative humidity (RH, unit: %); f. air-sea specific humidity difference (Δq , unit: g/kg); g. latent heat (LH, unit: W/m^2); h. sensible heat (SH, unit: W/m^2). Buoy A–H distributed along the path of tropical cyclone (TC) Danas from generation to extinction are labeled sequentially on the x-axis, and the TC Danas life cycle is shown on the y-axis. The outlines on the panels are isobars, where the white outlines in Fig.2a are the isoveLOCITY of 10 m/s, highlighting the significant effects of TC Danas, and the black outline is a 1000-hPa isobar to indicate the location of TC Danas.

intensified effect of high temperature and humidity at low latitudes. A rapid decrease in SST with increasing latitude led to a consequent decrease in the air-sea temperature and humidity difference. Despite a slight enhancement in WS, the mean values of LH and SH continued to decrease until they reached minimums of approximately 5.7 and $-12.7 \text{ W}/\text{m}^2$ at Buoy E, respectively. Buoy F, where extreme wind agitation was strongest, had the subhighest LH and SH values of 94 and $9.4 \text{ W}/\text{m}^2$, respectively. The lowest temperature and wind fields were measured by the high-latitude shore-side Buoy G, where LH and SH are -41 and $-28 \text{ W}/\text{m}^2$, respectively, indicating that the ocean extracted heat from the atmosphere. Thereafter, the increases in SST and WS caused by Danas were captured by Buoy H, at which time LH and SH were 2.6 and $-29 \text{ W}/\text{m}^2$, respectively. Accompanying the rare northward trajectory of Danas, the distribution of the THF anomaly field was characterized by a combination of the spindle-shaped structure of the wind field and the striped distribution of the SST field. The final representation of the THF anomaly field depended on the relative importance of wind

anomalies and humidity-related SST anomalies measured at different buoy stations.

The BLS was estimated using Eq.3 based on the observations of Buoy A–H. A lower air-sea temperature difference during the life cycle of Danas enables a near-neutral BLS to be dominant. The BLS was only stable at Buoy G, which is related to the fact that the SAT is larger than the nearshore SST. The physical mechanisms affecting the hourly THF anomalies in the same BLS state at a certain time are characterized by the following relationships:

$$Q_{\text{LH}}' = C_1 \left[\overline{u_z}' (\overline{\Delta q}) + \overline{u_z} (\Delta q)' + \overline{u_z}' (\Delta q)' \right], \quad (4)$$

$$Q_{\text{SH}}' = C_2 \left[\overline{u_z}' (\overline{\Delta T}) + \overline{u_z} (\Delta T)' + \overline{u_z}' (\Delta T)' \right], \quad (5)$$

where primes and overbars represent the anomalies (variables minus their average state) and the averages, respectively. The hourly THF anomaly terms on the lhs of Eqs.4 & 5 were decomposed into

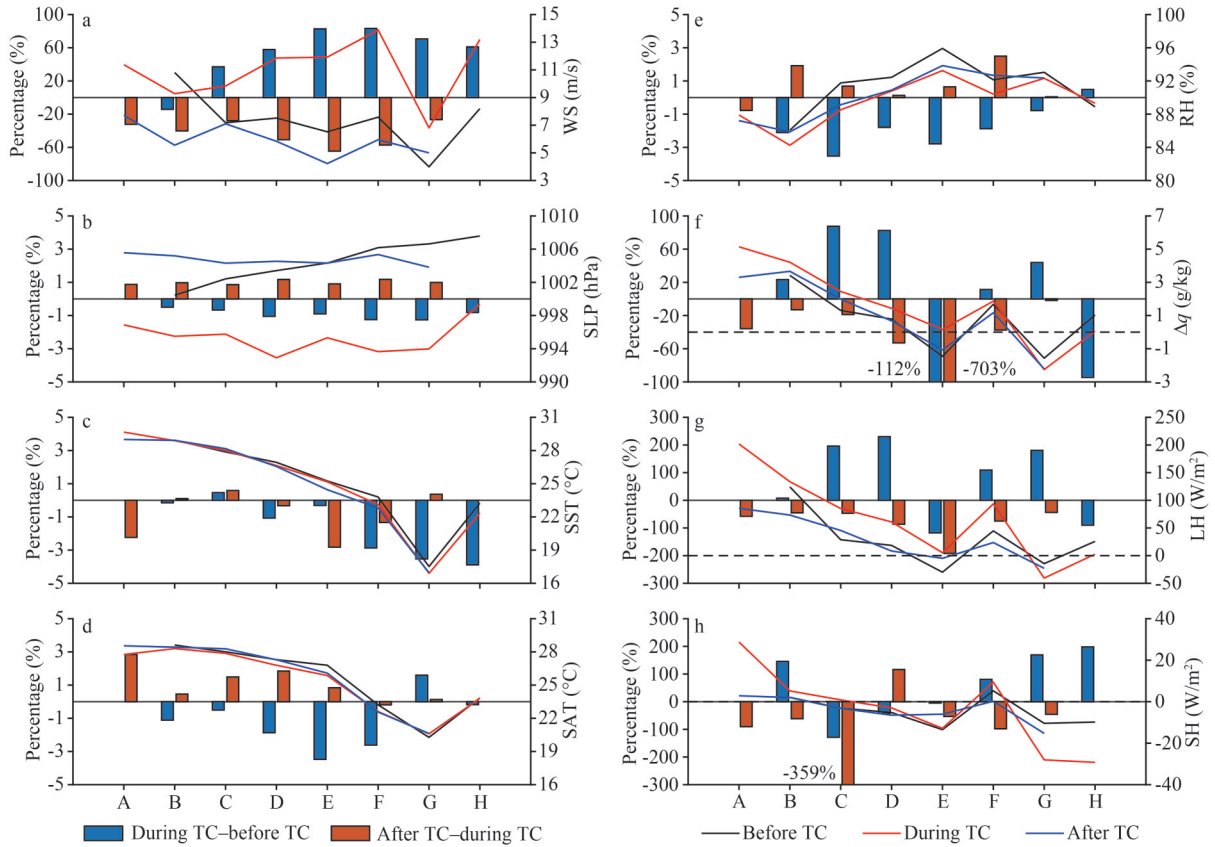


Fig.3 Bars of air-sea variable increase rates and time series of air-sea variable averages observed by Buoys A–H

Air-sea variables include (a) wind speed (WS, unit: m/s), (b) sea level pressure (SLP, unit: hPa), (c) sea surface temperature (SST, unit: °C), (d) surface air temperature (SAT, unit: °C), (e) relative humidity (RH, unit: %), (f) air-sea specific humidity difference (Δq , unit: g/kg), (g) latent heat (LH, unit: W/m^2), and (h) sensible heat (SH, unit: W/m^2). Black, red, and blue lines show the mean air-sea variables (right y-axis) before, during and after the passage of tropical cyclone (TC) Danas. Blue bars show the air-sea variable increase rates (left y-axis, unit: %), which are calculated as (value of the variable during the TC passage vs. value of the variable before the TC passage)/value of the variable before the TC passage \times 100%. Orange bars are the same as the blue bars, but for the increase in the air-sea variable after the TC passage relative to the air-sea variable during the TC passage. This study assumes that the period when the surface is below 1 000 hPa represents the period of the TC Danas passage.

the wind anomaly term (first term on the rhs), thermal anomaly term (second term on the rhs, namely, air-sea humidity and temperature difference anomaly terms) and nonlinear term (third term on the rhs) according to Eqs.1 & 2. Parameters C_1 and C_2 are set to the average of $\rho L_e C_E$ and $\rho C_p C_H$, respectively, over the selected sample duration to avoid parameter variations related to the air-sea interface state from interfering with the estimation of wind anomalies and thermal effect anomalies on the contribution of heat flux anomalies.

Figure 4 shows the hourly LH and SH anomalies, along with the hourly wind speed anomalies, thermal anomalies and nonlinear terms as potential contributors to the LH and SH anomalies. The associated correlation coefficients (R) are presented in Fig.5. The physical mechanism of the LH anomaly is constrained by the background field of

north-south transport of TC Danas across latitudes. At low latitudes with high temperature and humidity, the hourly LH anomalies are dominated by the wind anomalies (Fig.4a). The R -values associated with the wind anomalies are 0.80 and 0.95 during and after Danas passes Buoy A, respectively (Fig.5a). At Buoys B–C, as the latitude increases, there are conditions in the air-sea boundary layer where wind anomalies and air-sea specific humidity differences often alternately dominate hourly LH anomalies or even jointly dominate them during different periods, as shown in Figs.4a, 5a, & 5b. When reaching the higher latitudes where Buoy D–E are located, air-sea humidity anomalies began to be more closely related to LH anomalies, with R -values ranging from approximately 0.79–0.99 (Fig.5b), while wind anomalies played a secondary role in LH anomalies,

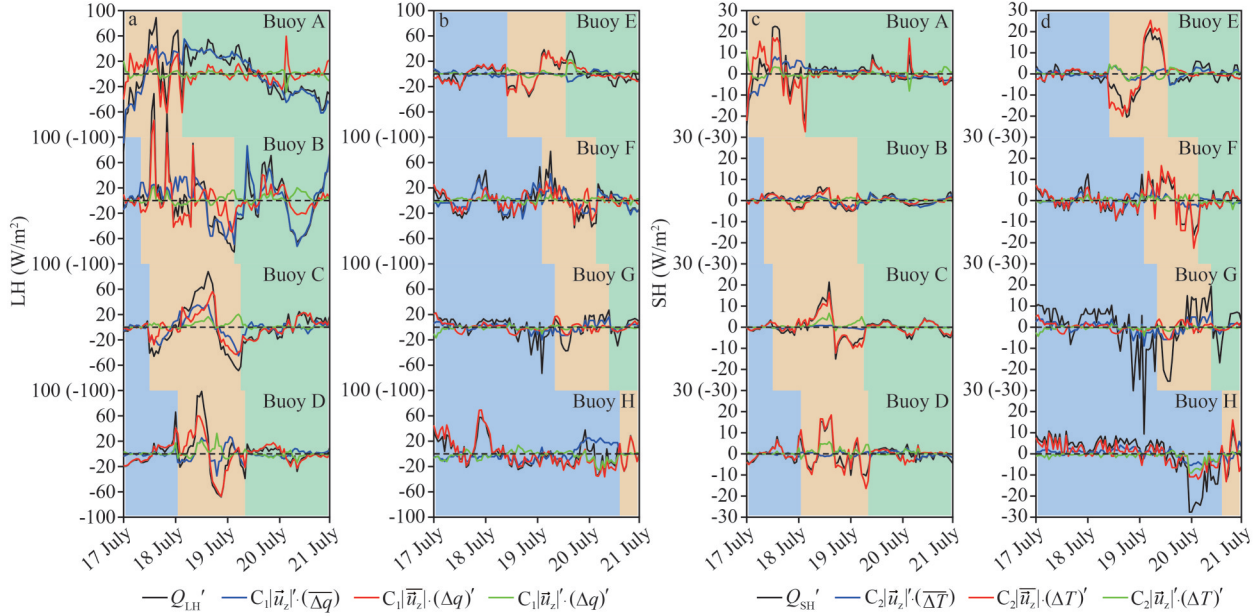


Fig.4 Time series of hourly LH and SH anomalies induced by air-sea variable anomalies at Buoys A–H

Black, blue, red and green lines indicate the latent heat (LH) anomaly term (Q_{LH}' in Eq.4), wind anomaly term ($C_1|\vec{u}_z|'(\Delta q)$ in Eq.4), air-sea specific humidity difference anomaly term ($C_1|\vec{u}_z|(\Delta q)'$ in Eq.4) and nonlinear term ($C_1|\vec{u}_z|'(\Delta q)'$ in Eq.4), respectively. The blue, yellow and green backgrounds in the panel represent the periods before, during and after the passage of TC Danas, respectively. The buoy station number is shown in the upper right corner of the panel. Panels c–d are the same as panels a–b, but for sensible heat (SH).

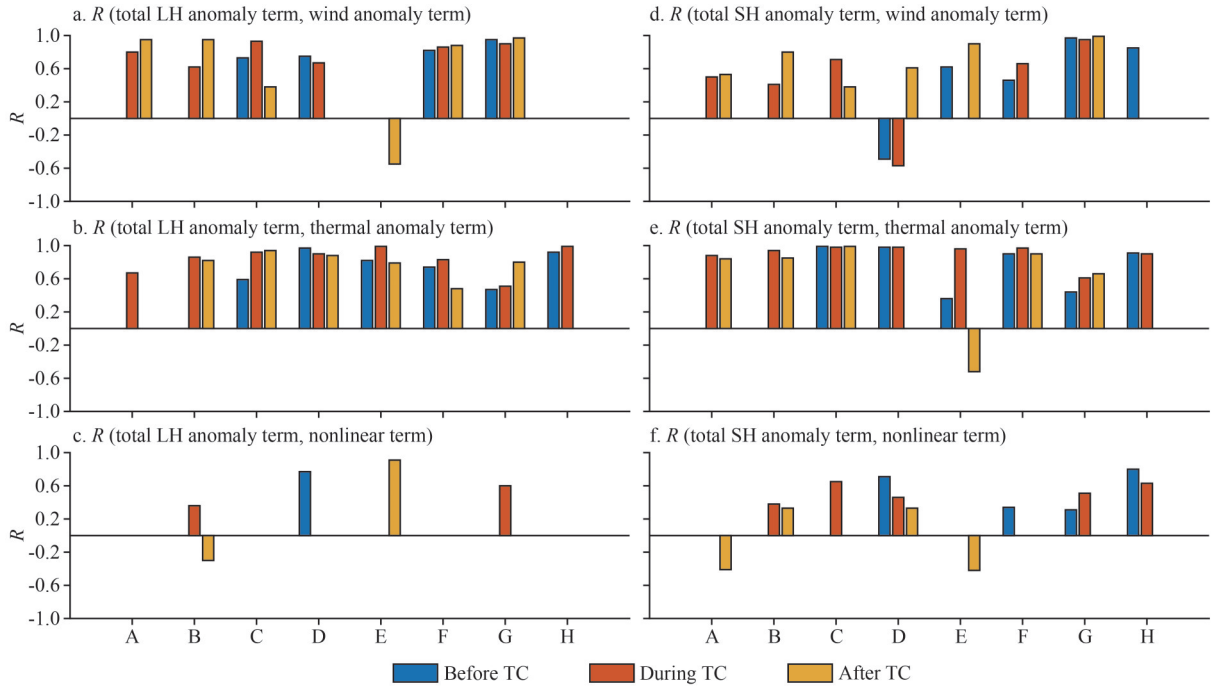


Fig.5 Correlation coefficients (R) between total flux anomaly terms and terms of flux anomalies induced by individual air-sea variable anomalies

The blue, red, and yellow bars represent the correlation coefficients associated with latent heat (LH, a–c) and sensible heat (SH, d–f) before, during and after the passage of tropical cyclone (TC) Danas, respectively. Negative R -values indicate opposite trends in time series changes. Absent bars represent a failure to pass the 95% confidence level or missing buoy measurements.

with R -values varying from approximately -0.55 – 0.75 (Fig.5a), regardless of whether BLS was near-neutral or stable. In contrast, at Buoy F, where the winds were strongest, and at Buoy G, near the shore, the LH anomalies are controlled by wind anomalies at any period (Fig.4b), with R -values of 0.82 – 0.97 , followed by humidity anomalies, with R -values of 0.48 – 0.83 . Finally, at Buoy H, which captured the Danas reentry process, the LH anomalies are most strongly linked to the air-sea specific humidity difference anomalies, with R -values of 0.92 and 0.99 before and during the passage of Danas, respectively (Figs.4b & 5b).

The estimates from the Buoys A–H observations indicate that the temperature anomalies have a stronger effect on the hourly SH anomalies than the wind speed anomalies and the nonlinear terms under near-neutral BLS conditions, especially during the passage of Danas. However, in the near-neutral air-sea boundary layer where Buoy D is located, the SH anomalies were dominated by wind anomalies with R -values of 0.61 after the passage of Danas (Figs.4c & 5d). The hourly SH anomalies in the sea surface where Buoy E is located were similarly dominated by wind anomalies before and after the passage of Danas, with R -values of 0.62 and 0.90 , respectively (Figs.4d & 5d), which may be explained by the increased stability of the marine atmospheric boundary layer. In addition, the sea surface where offshore Buoy G is located was also in stable conditions, so the SH anomalies were controlled by wind anomalies with R -values of 0.95 – 0.99 (Fig.5d), and the SST anomalies played a secondary role with R -values of 0.44 – 0.66 (Fig.5e).

3.2 Evaluation of reanalysis flux products ERA5 and MERRA2

To help improve forecast systems and reanalysis products, we focused on determining the largest sources of uncertainty and hence the largest differences between the buoy observations and reanalysis products. Specifically, to better understand the potential uncertainties in the reanalysis flux products in extreme environments at the air-sea interface induced by TC Danas, this section includes a comparison of the observations from Buoys A–H with the output of the ERA5 and MERRA2 reanalysis products after temporal and spatial matching. We found that the air-sea interface environments obtained from ERA5 and MERRA2 (Supplementary Figs.S1 & S2) reproduce the major features of those observed by the buoys (Fig.2), as

detailed in Supplementary File S1. However, there are some numerical differences in the air-sea state parameters between the reanalyses and observations (Supplementary Figs.S3 & S4). For example, the larger differences in THF between the reanalyses and observations are found at mainly the buoy sites with more extreme environments during the passage of Danas, as detailed in Supplementary File S2.

Figure 6 shows the correlation of air-sea variables between buoy observations and reanalysis products before, during and after the passage of Danas. This enables identification of the following three major features. First, in most cases, the correlation of air-sea variables between observations and reanalyses under calm weather conditions is higher than that under extreme cyclone conditions. This feature is not evident for the temperature and humidity terms that vary with latitude (Fig.2c–f), leading to correlation results for LH and SH that also do not reflect this feature, as shown in Fig.6g–h. Secondly, the ERA5 and MERRA2 products better simulate WS, SLP, and LH, while the temperature and humidity terms and SH are simulated less well. Specifically, for LH, Fig.6g shows that the correlation coefficients between ERA5 and observations are 0.69 , 0.80 , and 0.88 , and those between MERRA2 and observations are 0.37 , 0.67 , and 0.74 before, during, and after the passage of Danas, respectively. Thus, the simulation capability of the reanalysis for LH would be enhanced if the accuracy of air-sea variable observations in the extreme environment of high temperatures and strong winds, as well as in the complex environment of the nearshore, could be improved (Supplementary Figs.S3 & S4). For SH, Fig.6h shows that the R -values between ERA5 and the observations are 0.51 , 0.68 , and 0.43 , respectively, while none of the R -values between MERRA2 and the observations reach the 95% significance level, which may be related to the fact that the SH anomalies are dominated by the poorly modeled air-sea temperature difference anomalies (Figs.4c–d & 5e). Finally, because MERRA2 has a coarser spatial resolution than ERA5, ERA5 has a slightly better modeling capability than MERRA2 in most cases. For example, for the three periods, the R -values between ERA5 and observations reached 0.69 – 0.99 , 0.57 – 0.95 , and 0.80 – 0.96 , respectively, for all air-sea variables except SH, while the R -values between MERRA2 and observations were 0.37 – 0.97 , 0.56 – 0.91 , and 0.63 – 0.93 , respectively. The detailed correlation coefficients are shown in

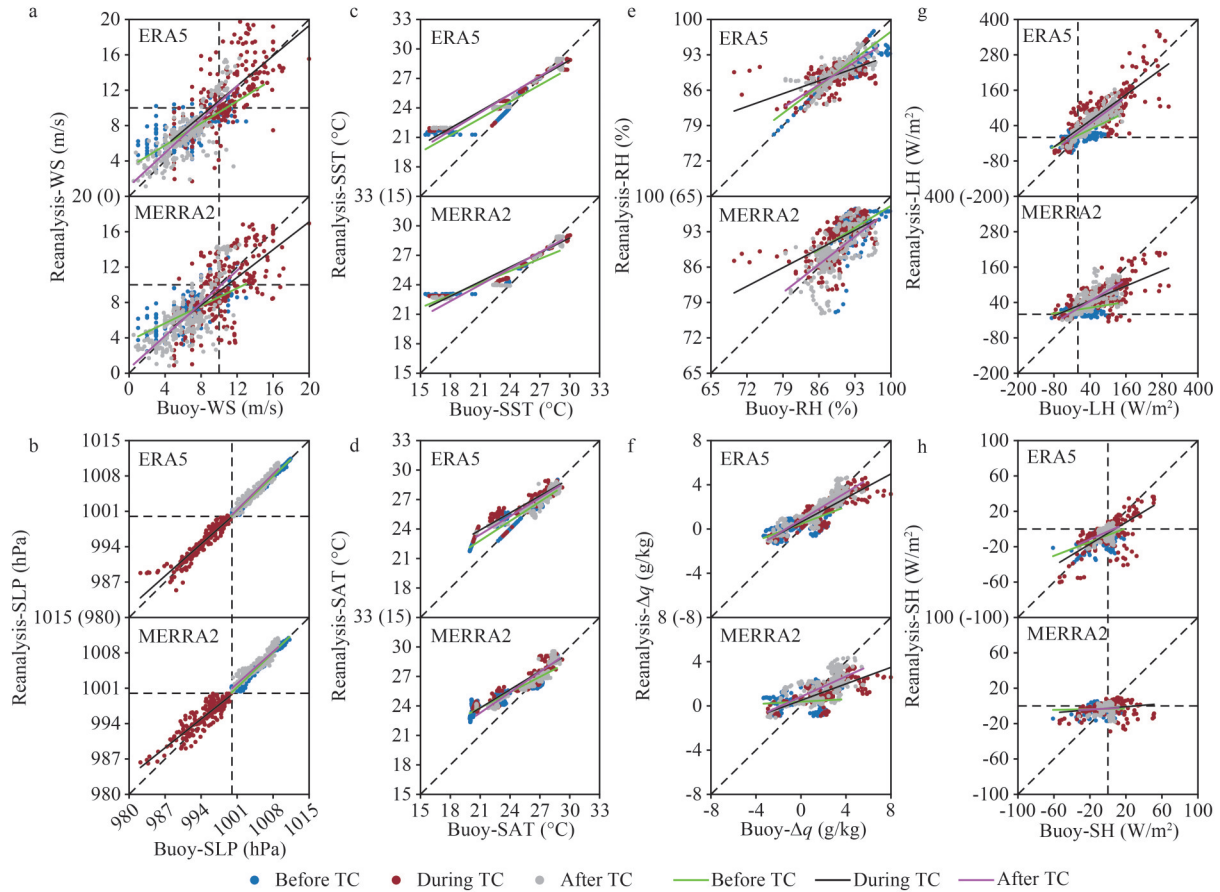


Fig.6 Comparison of air-sea variables from buoy observations and the ERA5 and MERRA2 reanalysis products

The blue, red, and gray dots represent the periods before, during, and after the passage of tropical cyclone (TC) Danas, respectively. Air-sea variables include wind speed (WS, unit: m/s) (a), sea level pressure (SLP, unit: hPa) (b), sea surface temperature (SST, unit: °C) (c), surface air temperature (SAT, unit: °C) (d), relative humidity (RH, unit: %) (e), air-sea specific humidity difference (Δq , unit: g/kg) (f), latent heat (LH, unit: W/m^2) (g), and sensible heat (SH, unit: W/m^2) (h). Linear regressions between buoy observations and reanalyses before, during, and after the passage of Danas are shown by green, black, and magenta solid lines, respectively. The black horizontal and vertical dashed lines indicate the values of the contours in Fig.2.

Supplementary File S3. In summary, more abundant and accurate high-resolution in-situ observations of temperature and humidity under extreme weather conditions have important implications for improving the ability of flux products to simulate LH and SH.

4 CONCLUSION

We investigated the extreme THF anomalies induced by TS Danas during July 17–21, 2019, using high-precision air-sea observations from multiple moored and drifting buoys. Unlike previous cases of TC observations by buoys, multiple buoy stations were used to capture the complete life cycle of Danas from its gradual maturation to its eventual dissipation, that is, from its longitudinal crossing of the ECS and the Yellow Sea to the Korean peninsula and finally to the Sea of Japan. Thus, we provided a more detailed evaluation

of the physical mechanisms of hourly LH and SH anomalies during the complete life cycle of Danas. Furthermore, exploiting the high-resolution observations, we also helped evaluate two state-of-the-art reanalysis flux products, i.e., ERA5 and MERRA2, and specifically assesses their capability to reproduce extreme THF. The major findings are summarized as follows.

First, During the passage of TC Danas (2019), there was a higher LH release from the ocean to the atmosphere and enhanced SH exchanges at the interface due to the combination of extreme winds greater than 10 m/s and varying temperature and humidity fields with latitude. Almost all buoy-based marine atmospheric boundary layer conditions are dominated by near-neutral conditions. The physical mechanism of hourly LH anomalies is related to latitude. LH anomalies measured by the low-latitude buoy are dominated by wind anomalies. With

increasing latitude, the LH anomalies measured by the buoys are gradually controlled by wind anomalies and air-sea humidity anomalies alternately or even jointly. Finally, they are well controlled by the air-sea specific humidity difference anomalies. However, the driver of the LH anomalies at the strongest wind station and the nearshore station, which are at higher latitudes, is the wind speed. In addition, the physical mechanism of hourly SH anomalies is related to boundary stability. The hourly SH anomalies depend on air-sea temperature anomalies under near-neutral conditions, while those under stable conditions are controlled by wind anomalies.

Secondly, the reanalysis products ERA5 and MERRA2 basically reproduce the major features and evolution of the air-sea parameters compared to the buoy observations. However, discrepancies exist in the detailed amplitude and variability between the reanalyzed and observed air-sea parameters. (i) Although the WS and SLP have larger errors between the reanalyses and observations during the passage of Danas, the LH and SH do not reflect this feature because the temperature and humidity terms are mainly affected by latitude. (ii) The reanalysis products simulate the WS, SLP and LH better than the temperature and humidity terms and the SH. (iii) ERA5 with higher spatial resolution has better simulation capabilities. For LH, the correlation coefficients between ERA5 (MERRA2) and observations were 0.69 (0.37), 0.80 (0.67), and 0.88 (0.74) before, during and after the passage of Danas, respectively; for SH, the R -values between ERA5 and observations were 0.51, 0.68, and 0.43, respectively, while the correlation coefficients between MERRA2 and observations failed to reach the 95% significance level. The low and nonsignificant correlations imply a slightly poor representation of the THF during TCs by MERRA2.

In summary, WS and SST anomalies play a major role in controlling LH and SH anomalies. Multisource, high-resolution in-situ observations of temperature and humidity under extreme weather conditions will provide new directions for improving reanalysis flux products. Specifically, an integrated observational network of air-sea variables from the basin to the global scale would provide a more comprehensive and complete set of observations, which in turn would inform the development of semiempirical parameterization algorithms. To ensure the efficiency of operational marine meteorological forecasts, the Louis 79

scheme (Louis, 1979) is widely used for estimating the surface fluxes in reanalysis products. We obtained recalculated fluxes based on the reanalyzed air-sea variables using the COARE 3.5 algorithm and compared them to the original reanalyzed fluxes (Supplementary Fig.S5). The results show that ERA5, which has a higher resolution and thus captures more detail, has a larger error due to different parameterization algorithms in response to small- and medium-scale TS Danas passages. Therefore, improved parameterization algorithms may be an effective and necessary way to obtain a new generation of high-resolution global flux products that will better resolve the global heat balance imbalance. In addition, they will contribute to improved predictions of TC development and intensification, helping to prevent future damage.

5 DATA AVAILABILITY STATEMENT

The observation data can be found on the NDBC website (<https://www.ndbc.noaa.gov/>). Typhoon track data can be downloaded from the IBTrACS website (<https://www.ncdc.noaa.gov/ibtracs/>). The atmospheric reanalysis data can be downloaded from the ERA5 website (<https://www.ecmwf.int>) and the MERRA2 website (<https://gmao.gsfc.nasa.gov/>).

6 ACKNOWLEDGMENT

The authors appreciate the anonymous reviewers for their constructive comments.

References

- Bell B, Hersbach H, Simmons A et al. 2021. The ERA5 global reanalysis: preliminary extension to 1950. *Quarterly Journal of the Royal Meteorological Society*, **147**(741): 4186-4227, <https://doi.org/10.1002/qj.4174>.
- Bracken W E, Bosart L F. 2000. The role of synoptic-scale flow during tropical cyclogenesis over the North Atlantic Ocean. *Monthly Weather Review*, **128**(2): 353-376, [https://doi.org/10.1175/1520-0493\(2000\)128<0353:TROSSF>2.0.CO;2](https://doi.org/10.1175/1520-0493(2000)128<0353:TROSSF>2.0.CO;2).
- Centurioni L R, Turton J, Lumpkin R et al. 2019. Global *in situ* observations of essential climate and ocean variables at the air-sea interface. *Frontiers in Marine Science*, **6**: 419, <https://doi.org/10.3389/fmars.2019.00419>.
- Cronin M F, Gentemann C L, Edson J et al. 2019. Air-sea fluxes with a focus on heat and momentum. *Frontiers in Marine Science*, **6**: 403, <https://doi.org/10.3389/fmars.2019.00430>.
- D'Asaro E A, Sanford T B, Niiler P P et al. 2007. Cold wake of Hurricane Frances. *Geophysical Research Letters*,

- 34(15): L15609, <https://doi.org/10.1029/2007GL030160>.
- Dare R A, McBride J L. 2011. The threshold sea surface temperature condition for tropical cyclogenesis. *Journal of Climate*, **24**(17): 4570-4576, <https://doi.org/10.1175/JCLI-D-10-05006.1>.
- Dee D P, Uppala S M, Simmons A J et al. 2011. The ERA-Interim reanalysis: configuration and performance of the data assimilation system. *Quarterly Journal of the Royal Meteorological Society*, **137**(656): 553-597, <https://doi.org/10.1002/qj.828>.
- DeMaria M, Mainelli M, Shay L K et al. 2005. Further improvements to the Statistical Hurricane Intensity Prediction Scheme (SHIPS). *Weather and Forecasting*, **20**(4): 531-543, <https://doi.org/10.1175/WAF862.1>.
- DeMaria M, Sampson C R, Knaff J A et al. 2014. Is tropical cyclone intensity guidance improving? *Bulletin of the American Meteorological Society*, **95**(3): 387-398, <https://doi.org/10.1175/BAMS-D-12-00240.1>.
- Edson J B, Jampana V, Weller R A et al. 2013. On the exchange of momentum over the open ocean. *Journal of Physical Oceanography*, **43**(8): 1589-1610, <https://doi.org/10.1175/JPO-D-12-0173.1>.
- Emanuel K A. 1986. An air-sea interaction theory for tropical cyclones. Part I: steady-state maintenance. *Journal of the Atmospheric Sciences*, **43**(6): 585-605, [https://doi.org/10.1175/1520-0469\(1986\)043<0585:AASITF>2.0.CO;2](https://doi.org/10.1175/1520-0469(1986)043<0585:AASITF>2.0.CO;2).
- Emanuel K A. 1995. Sensitivity of tropical cyclones to surface exchange coefficients and a revised steady-state model incorporating eye dynamics. *Journal of the Atmospheric Sciences*, **52**(22): 3969-3976, [https://doi.org/10.1175/1520-0469\(1995\)052<3969:SOTCTS>2.0.CO;2](https://doi.org/10.1175/1520-0469(1995)052<3969:SOTCTS>2.0.CO;2).
- Fairall C W, Bradley E F, Hare J E et al. 2003. Bulk parameterization of air-sea fluxes: updates and verification for the COARE algorithm. *Journal of Climate*, **16**(4): 571-591, [https://doi.org/10.1175/1520-0442\(2003\)016<0571:BPOASF>2.0.CO;2](https://doi.org/10.1175/1520-0442(2003)016<0571:BPOASF>2.0.CO;2).
- Fairall C W, Bradley E F, Rogers D P et al. 1996. Bulk parameterization of air-sea fluxes for Tropical Ocean-Global Atmosphere Coupled-Ocean Atmosphere Response Experiment. *Journal of Geophysical Research: Oceans*, **101**(C2): 3747-3764, <https://doi.org/10.1029/95JC03205>.
- Garrison D L, Gowing M M, Hughes M P et al. 2000. Microbial food web structure in the Arabian Sea: a US JGOFS study. *Deep Sea Research Part II: Topical Studies in Oceanography*, **47**(7-8): 1387-1422, [https://doi.org/10.1016/S0967-0645\(99\)00148-4](https://doi.org/10.1016/S0967-0645(99)00148-4).
- Gelaro R, McCarty W, Suárez M J et al. 2017. The modern-era retrospective analysis for research and applications, version 2 (MERRA-2). *Journal of Climate*, **30**(14): 5419-5454, <https://doi.org/10.1175/JCLI-D-16-0758.1>.
- Godfrey J S, Beljaars A C M. 1991. On the turbulent fluxes of buoyancy, heat and moisture at the air-sea interface at low wind speeds. *Journal of Geophysical Research*, **96**(C12): 22043-22048, <https://doi.org/10.1029/91JC02015>.
- Goerss J S, Sampson C R, Gross J M. 2004. A history of western North Pacific tropical cyclone track forecast skill. *Weather and Forecasting*, **19**(3): 633-638, [https://doi.org/10.1175/1520-0434\(2004\)019<0633:AHOWNP>2.0.CO;2](https://doi.org/10.1175/1520-0434(2004)019<0633:AHOWNP>2.0.CO;2).
- Hersbach H, Bell B, Berrisford P et al. 2020. The ERA5 global reanalysis. *Quarterly Journal of the Royal Meteorological Society*, **146**(730): 1999-2049, <https://doi.org/10.1002/qj.3803>.
- Hubbert G D, Holland G J, Leslie L M et al. 1991. A real-time system for forecasting tropical cyclone storm surges. *Weather and Forecasting*, **6**(1): 86-97, [https://doi.org/10.1175/1520-0434\(1991\)006<0086:ARTSFF>2.0.CO;2](https://doi.org/10.1175/1520-0434(1991)006<0086:ARTSFF>2.0.CO;2).
- Jayakrishnan K U, Kutty G, George B. 2020. On the predictability and dynamics of tropical cyclone: Nargis (2008). *Journal of Geophysical Research: Atmospheres*, **125**(9): e2019JD032040, <https://doi.org/10.1029/2019JD032040>.
- Karnauskas K B, Zhang L, Emanuel K A. 2021. The feedback of cold wakes on tropical cyclones. *Geophysical Research Letters*, **48**(7): e2020GL091676, <https://doi.org/10.1029/2020GL091676>.
- Keptert J D, Ginger J D. 2010. Guidelines for Converting between Various Wind Averaging Periods in Tropical Cyclone Conditions. World Meteorological Organization, Geneva, https://library.wmo.int/index.php?lvl=notice_display&id=135.
- Khouakhi A, Villarini G, Vecchi G A. 2017. Contribution of tropical cyclones to rainfall at the global scale. *Journal of Climate*, **30**(1): 359-372, <https://doi.org/10.1175/JCLI-D-16-0298.1>.
- Knapp K R, Kruk M C, Levinson D H et al. 2010. The international best track archive for climate stewardship (IBTrACS). *Bulletin of the American Meteorological Society*, **91**(3): 363-376, <https://doi.org/10.1175/2009BAMS2755.1>.
- Komori S, Iwano K, Takagaki N et al. 2018. Laboratory measurements of heat transfer and drag coefficients at extremely high wind speeds. *Journal of Physical Oceanography*, **48**(4): 959-974, <https://doi.org/10.1175/JPO-D-17-0243.1>.
- Landsea C W, Cangialosi J P. 2018. Have we reached the limits of predictability for tropical cyclone track forecasting? *Bulletin of the American Meteorological Society*, **99**(11): 2237-2243, <https://doi.org/10.1175/BAMS-D-17-0136.1>.
- Landwehr S, O'Sullivan N, Ward B. 2015. Direct flux measurements from mobile platforms at sea: motion and airflow distortion corrections revisited. *Journal of Atmospheric and Oceanic Technology*, **32**(6): 1163-1178, <https://doi.org/10.1175/JTECH-D-14-00137.1>.
- Lin I I, Chen C H, Pun I F et al. 2009. Warm ocean anomaly, air sea Fluxes, and the rapid intensification of tropical cyclone Nargis (2008). *Geophysical Research Letters*, **36**(3): L03817, <https://doi.org/10.1029/2008GL035815>.
- Liu W T, Katsaros K B, Businger J A. 1979. Bulk parameterization of air-sea exchanges of heat and water vapor including the molecular constraints at the interface. *Journal of the Atmospheric Sciences*, **36**(9): 1722-1735, [https://doi.org/10.1175/1520-0469\(1979\)036<1722:BPOASE>2.0.CO;2](https://doi.org/10.1175/1520-0469(1979)036<1722:BPOASE>2.0.CO;2).

- Liu W T, Tang W Q. 2016. Relating wind and stress under tropical cyclones with scatterometer. *Journal of Atmospheric and Oceanic Technology*, **33**(6): 1151-1158, <https://doi.org/10.1175/JTECH-D-16-0047.1>.
- Louis J F. 1979. A parametric model of vertical eddy fluxes in the atmosphere. *Boundary-Layer Meteorology*, **17**(2): 187-202, <https://doi.org/10.1007/BF00117978>.
- Ma Z H, Fei J F, Huang X et al. 2015. Contributions of surface sensible heat fluxes to tropical cyclone. Part I: evolution of tropical cyclone intensity and structure. *Journal of the Atmospheric Sciences*, **72**(1): 120-140, <https://doi.org/10.1175/JAS-D-14-0199.1>.
- Ma Z H, Fei J F, Lin Y L et al. 2020. Modulation of clouds and rainfall by tropical cyclone's cold wakes. *Geophysical Research Letters*, **47**(17): e2020GL088873, <https://doi.org/10.1029/2020GL088873>.
- Malkus J S, Riehl H. 1960. On the dynamics and energy transformations in steady-state hurricanes. *Tellus A: Dynamic Meteorology and Oceanography*, **12**(1): 1-20, <https://doi.org/10.3402/tellusa.v12i1.9351>.
- Malone T C. 2003. The coastal module of the Global Ocean Observing System (GOOS): an assessment of current capabilities to detect change. *Marine Policy*, **27**(4): 295-302, [https://doi.org/10.1016/S0308-597X\(03\)00043-5](https://doi.org/10.1016/S0308-597X(03)00043-5).
- Marks Jr F D, Houze Jr R A. 1987. Inner core structure of Hurricane Alicia from airborne Doppler radar observations. *Journal of the Atmospheric Sciences*, **44**(9): 1296-1317, [https://doi.org/10.1175/1520-0469\(1987\)044<1296:ICSOHA>2.0.CO;2](https://doi.org/10.1175/1520-0469(1987)044<1296:ICSOHA>2.0.CO;2).
- McPhaden M J. 1995. The tropical atmosphere ocean array is completed. *Bulletin of the American Meteorological Society*, **76**(5): 739-744, <https://doi.org/10.1175/1520-0477-76.5.739>.
- McTaggart-Cowan R, Davies E L, Fairman Jr J G et al. 2015. Revisiting the 26.5 °C sea surface temperature threshold for tropical cyclone development. *Bulletin of the American Meteorological Society*, **96**(11): 1929-1943, <https://doi.org/10.1175/BAMS-D-13-00254.1>.
- Monin A S, Obukhov A M. 1954. Basic regularity in turbulent mixing in surface layer of the atmosphere. *Trudy Geofiz, Instituta Akademii Nauk, SSSR (Proceedings of Geophysics Institute, National Academy of Science, SSSR)*, **24**(151): 163-187, https://gibbs.science/efd/handouts/monin_obukhov_1954.pdf.
- Needham H F, Keim B D. 2014. An empirical analysis on the relationship between tropical cyclone size and storm surge heights along the U.S. gulf coast. *Earth Interactions*, **18**(8): 1-15, <https://doi.org/10.1175/2013EI000558.1>.
- NOAA Office for Coastal Management. 2023. Tropical cyclones: the highest costs. Fast facts, Hurricane costs, August 2023, <https://coast.noaa.gov/states/fast-facts/hurricane-costs.html>. Accessed on 2023-11-19.
- Powell M D, Reinhold T A. 2007. Tropical cyclone destructive potential by integrated kinetic energy. *Bulletin of the American Meteorological Society*, **88**(4): 513-526, <https://doi.org/10.1175/BAMS-88-4-513>.
- Price J F. 1981. Upper ocean response to a hurricane. *Journal of Physical Oceanography*, **11**(2): 153-175, [https://doi.org/10.1175/1520-0485\(1981\)011<0153:UORTAH>2.0.CO;2](https://doi.org/10.1175/1520-0485(1981)011<0153:UORTAH>2.0.CO;2).
- Price J F, Morzel J, Niiler P P. 2008. Warming of SST in the cool wake of a moving hurricane. *Journal of Geophysical Research: Oceans*, **113**(C7): C07010, <https://doi.org/10.1029/2007JC004393>.
- Rodgers E B, Baik J J, Pierce H F. 1994. The environmental influence on tropical cyclone precipitation. *Journal of Applied Meteorology and Climatology*, **33**(5): 573-593, [https://doi.org/10.1175/1520-0450\(1994\)033<0573:TEIOTC>2.0.CO;2](https://doi.org/10.1175/1520-0450(1994)033<0573:TEIOTC>2.0.CO;2).
- Scharroo R, Smith W H F, Lillibridge J L. 2005. Satellite altimetry and the intensification of Hurricane Katrina. *Eos, Transactions American Geophysical Union*, **86**(40): 366-366, <https://doi.org/10.1029/2005EO400004>.
- Schultz C. 2011. Surface ocean-lower atmosphere processes. *Eos, Transactions American Geophysical Union*, **92**(7): 57-57, <https://doi.org/10.1029/2011EO070009>.
- Smith N, Kessler W S, Cravatte S et al. 2019. Tropical pacific observing system. *Frontiers in Marine Science*, **6**: 31, <https://doi.org/10.3389/fmars.2019.00031>.
- Song X Z. 2020. The importance of relative wind speed in estimating air-sea turbulent heat fluxes in bulk formulas: examples in the Bohai Sea. *Journal of Atmospheric and Oceanic Technology*, **37**(4): 589-603, <https://doi.org/10.1175/JTECH-D-19-0091.1>.
- Song X Z, Ning C L, Duan Y L et al. 2021. Observed extreme air-sea heat flux variations during three tropical cyclones in the tropical southeastern Indian Ocean. *Journal of Climate*, **34**(9): 3683-3705, <https://doi.org/10.1175/JCLI-D-20-0170.1>.
- Stramma L, Cornillon P, Price J F. 1986. Satellite observations of sea surface cooling by hurricanes. *Journal of Geophysical Research: Oceans*, **91**(C4): 5031-5035, <https://doi.org/10.1029/JC091iC04p05031>.
- Xie X H, Wei Z X, Wang B et al. 2022. Extreme air-sea turbulent fluxes during tropical cyclone Barijat observed by a newly designed drifting buoy. *Fundamental Research*, published Online on September 2022. <https://doi.org/10.1016/j.fmre.2022.08.022>.
- Yelland M J, Moat B I, Taylor P K et al. 1998. Wind stress measurements from the open ocean corrected for airflow distortion by the ship. *Journal of Physical Oceanography*, **28**(7): 1511-1526, [https://doi.org/10.1175/1520-0485\(1998\)028<1511:WSMFTO>2.0.CO;2](https://doi.org/10.1175/1520-0485(1998)028<1511:WSMFTO>2.0.CO;2).
- Zhang F Q, Sippel J A. 2009. Effects of moist convection on hurricane predictability. *Journal of the Atmospheric Sciences*, **66**(7): 1944-1961, <https://doi.org/10.1175/2009JAS2824.1>.

Electronic supplementary material

Supplementary material (Supplementary Figs.S1–S5 and Files S1–S4) is available in the online version of this article at <https://doi.org/10.1007/s00343-024-3192-z>.